
CHALMERS
UNIVERSITY OF TECHNOLOGY

# Fluid-structure interaction of a triple-wingsail system

7th International Conference on Innovation in High Performance Sailing Yachts and Wind Assisted Ships. InnovSail 2026, Gothenburg, Sweden, 3-5 June 2026.

# Fluid-structure interaction of a triple-wingsail system

**Heng Zhu**
Chalmers University of Technology, Department of Mechanics and Maritime Sciences, Division of Marine Technology, Gothenburg 41296, Sweden. Corresponding author: heng.zhu@chalmers.se

**Clara Tous**
Chalmers University of Technology, Department of Mechanics and Maritime Sciences, Division of Marine Technology, Gothenburg 41296, Sweden.

**Glódís Hermannsdóttir**
Chalmers University of Technology, Department of Mechanics and Maritime Sciences, Division of Marine Technology, Gothenburg 41296, Sweden.

**Hua-Dong Yao**
Chalmers University of Technology, Department of Mechanics and Maritime Sciences, Division of Marine Technology, Gothenburg 41296, Sweden.

## Abstract

Wind-assisted ship propulsion (WASP) using rigid wingsails has attracted increasing attention as a promising approach for reducing fuel consumption and greenhouse gas (GHG) emissions in maritime transport. While previous studies mainly focused on the aerodynamic performance of individual sails, the aeroelastic behavior and aerodynamic interaction of multiple wingsails remain insufficiently understood. This study investigates the fluid–structure interaction (FSI) of a triple-wingsail system using a two-way coupled framework. The aerodynamic flow field is simulated using computational fluid dynamics (CFD) with an improved delayed detached-eddy simulation (IDDES), while the structural response of the wingsails is computed using dynamic finite element analysis (FEA). Three apparent wind angles (β = 60°, 90°, and 120°) are examined. The results show that the upstream wingsail experiences larger deformation due to wake interaction from downstream wingsails. The dominant structural oscillation frequency is close to the natural frequency of the wingsail, indicating strong aeroelastic coupling. Aeroelastic deformation slightly modifies the lift coefficients but has a more noticeable influence on drag and load distribution along the wingsail span. These findings improve the understanding of aeroelastic effects in multi-wingsail propulsion systems.

**Keywords:** aeroelasticity; fluid–structure interaction; wind-assisted ship propulsion; wingsail

## NOMENCLATURE

| | |
|---|---|
| $C$ | Damping matrix |
| $C_D$ | Drag coefficient [-] |
| $C_L$ | Lift coefficient [-] |
| $C_M$ | Moment coefficient [-] |
| $F$ | Total aerodynamic force [N] |
| $K$ | Stiffness matrix |
| $L_c$ | Chord length [m] |
| $L_s$ | Spanwise length [m] |
| $M$ | Mass matrix |

| | |
|---|---|
| $p$ | Relative pressure [$\mathrm{Pa}$] |
| $Q$ | Q-criterion [$\mathrm{s}^{-2}$] |
| $Re$ | Reynolds number [-] |
| $t$ | Time [s] |
| $V_\infty$ | Freestream velocity magnitude [$\mathrm{m/s}$] |
| $y^+$ | Dimensionless wall distance [-] |
| $\alpha$ | Angle of attack [°] |
| $\beta$ | Apparent wind angle [°] |
| $\lambda$ | Displacement [$\mathrm{m}$] |
| $\rho$ | Air density [$\mathrm{kg \cdot m^{-3}}$] |

| | |
|---|---|
| CFD | Computational Fluid Dynamics |
| CFL | Courant–Friedrichs–Lewy |
| FEA | Finite Element Analysis |
| FSI | Fluid–Structure Interaction |
| GHG | Greenhouse Gas |
| IDDES | Improved Delayed Detached Eddy Simulation |
| LES | Large Eddy Simulation |
| RANS | Reynolds-Averaged Navier–Stokes |
| WASP | Wind-Assisted Ship Propulsion |

## 1. Introduction

The maritime transport sector plays a critical role in global trade but is also responsible for a significant share of greenhouse gas emissions. According to the International Maritime Organization (IMO), international shipping accounted for approximately $3\%$ of global $CO_2$ emissions in 2018 and substantial reductions are required to meet long-term decarbonization targets (IMO, 2023). Consequently, increasing attention has been directed toward wind-assisted ship propulsion (WASP) technologies as a practical approach to reduce fuel consumption and emissions from large commercial vessels (Huang & Souppez, 2025; Lu & Ringsberg, 2020; Reche-Vilanova *et al.*, 2021; Thies & Fakiolas, 2022).

Among the various WASP concepts, rigid wingsails have attracted considerable interest due to their high aerodynamic efficiency and their ability to generate thrust across a wide range of wind directions (Persson *et al.*, 2019; Zhu *et al.*, 2023c). Compared with traditional soft sails, wingsails can provide higher lift-to-drag ratios and more stable aerodynamic performance. In particular, cambered wingsail concepts such as crescent-shaped profiles have demonstrated improved thrust generation compared with conventional symmetric airfoil sails (Atkinson, 2019; Ouchi *et al.*, 2011; Zeng *et al.*, 2023; Zhang *et al.*, 2023; Zhu *et al.*, 2023c). For instance, some studies reported that optimized sail operation strategies can increase the thrust coefficient and reduce fuel consumption by more than $5\%$ in practical shipping routes (Engström *et al.*, 2025; Lu & Ringsberg, 2020; Zhang *et al.*, 2025; Zhu *et al.*, 2023c). These characteristics make wingsails a promising technology for practical deployment on commercial ships.

Previous studies have mainly focused on the aerodynamic performance of individual wingsails, including the influence of airfoil geometry, operating conditions, and Reynolds number effects (Souppez, 2023; Thies & Fakiolas, 2022; Zhu, 2024). Numerical simulations and wind-tunnel experiments have been widely used to evaluate lift, drag, and thrust characteristics of different wingsail concepts (Hillenbrand *et al.*, 2024; Xu *et al.*, 2025; Zhu *et al.*, 2023b; Zhu *et al.*, 2024b). However, real ships typically install multiple wingsails to achieve meaningful propulsion power (Ma *et al.*, 2025; Malmek *et al.*, 2024; van Reen *et al.*, 2025; Zhang *et al.*, 2024; Zhu *et al.*, 2023b). In such multi-sail configurations, aerodynamic interference between sails becomes important. The wake generated by upstream sails alters the inflow conditions of downstream sails, leading to changes in lift, drag, and overall propulsion efficiency.

Another important aspect that has received limited attention is the aeroelastic behavior of wingsails. To reduce structural weight and minimize impacts on ship stability and cargo capacity, wingsails are generally designed as lightweight and slender structures (Zhu *et al.*, 2023a). Under strong aerodynamic loading, these structures may experience noticeable deformation (Mebratu *et al.*, 2026; Ouchi *et al.*, 2013; Storhaug *et al.*, 2022; Zhu *et al.*, 2024a). Such structural deflections can in turn modify the local angle of attack and aerodynamic loading, resulting in fluid–structure interaction (FSI) effects. Previous investigations of wingsail structures have largely relied on static or quasi-static finite element analysis, which cannot capture the dynamic coupling between the flow field and structural deformation (Hu *et al.*, 2015; Zhu *et al.*, 2023a).

Despite these advances, it is important to distinguish between the scope of previous studies by the authors and the contributions of the present work. Previous investigations have focused on (i) the aerodynamic performance of single crescent-shaped wingsails, including Reynolds number sensitivity and flow separation mechanisms, and (ii) the aeroelastic behavior of an isolated wingsail using two-way coupled FSI approaches. However, these studies were limited to single-sail configurations and did not account for aerodynamic interaction between multiple wingsails. In practical ship applications, wingsails are installed in arrays, where wake interaction and flow interference can significantly alter both aerodynamic loading and structural response.

The present study extends beyond previous work by investigating, for the first time, the coupled aeroelastic behavior of a multi-wingsail system. Specifically, a triple-wingsail configuration is analyzed using a two-way coupled CFD–FEA framework, enabling the simultaneous examination of (i) aerodynamic interaction between sails, (ii) deformation-induced flow modification, and (iii) the resulting redistribution of aerodynamic loads within the sail array. This combined treatment of aerodynamic interference and aeroelastic coupling represents a key distinction from prior single-sail studies and provides new insight into the behavior of realistic multi-wingsail propulsion systems.

## 2. Methods

### 2.1 Design

The concept design of the triple-wingsail system investigated in this study is illustrated in **Figure 1**. The system consists of three identical rigid wingsails installed along the centerline of a large commercial vessel.

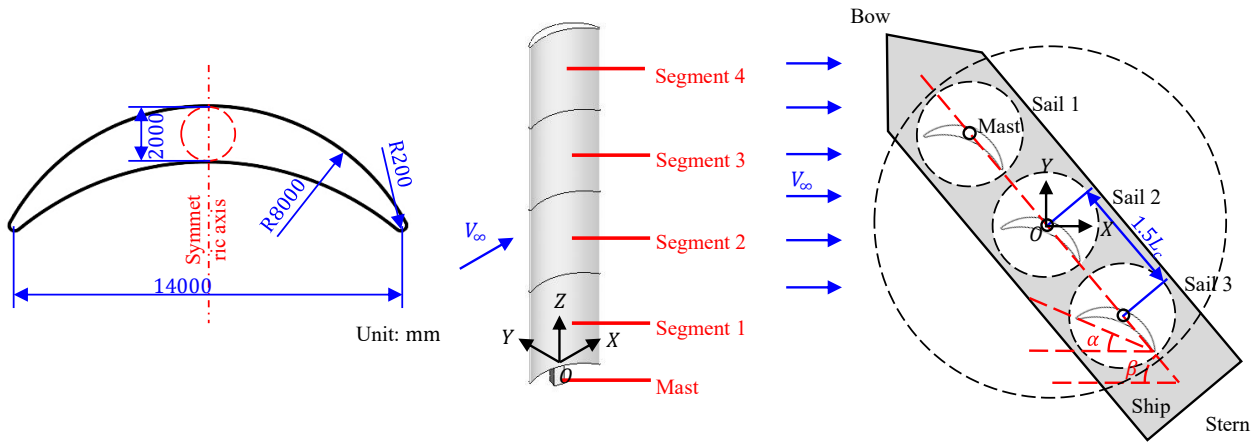


(a) Horizontal section of the wingsail profile. (b) Vertical segments and mast of the wingsail structure. (c) Triple-wingsail arrangement.

**Figure 1**. Concept design of the triple-wingsail system.

The sectional geometry of the wingsail is based on a crescent-shaped profile, as shown in **Figure 1**(a). The profile is generated using circular arcs to achieve a cambered aerodynamic shape while maintaining geometric simplicity (Zhu *et al.*, 2024b). The chord length ($L_c$) of the profile is $14\ \mathrm{m}$. The mast diameter is $2\ \mathrm{m}$, and the suction-side curvature is defined by an arc with a radius of $8\ \mathrm{m}$. The edges of the profile are rounded with a radius of $0.2\ \mathrm{m}$ to avoid sharp discontinuities and to improve aerodynamic behavior. The profile is symmetric with respect to the mid-chord axis, which allows the sail to operate efficiently under both port and starboard wind conditions (Zhu, 2023).

Each wingsail is designed as a vertically telescopic structure consisting of four segments, as shown in **Figure 1**(b). These segments are denoted as Segment 1 to Segment 4 from the bottom to the top of the sail (Zhu *et al.*, 2023a). The telescopic design allows the wingsail height to be adjusted depending on wind conditions and operational requirements. In the present study, the wingsail is considered in fully expanded configuration. A coordinate system is defined with the $X$-axis aligned with the incoming flow direction, the $Y$-axis in the lateral direction, and the $Z$-axis pointing vertically along the spanwise direction of the sail.

The installation layout of the three sails is illustrated in **Figure 1**(c). The sails are arranged in an in-line configuration along the longitudinal axis of the ship (van Reen *et al.*, 2025; Zhu *et al.*, 2023b). The distance between adjacent sails is set to $1.5L_c$. The aerodynamic performance of the system is evaluated under different apparent wind angles $\beta$ ($60°$, $90°$, and $120°$) and a fixed angle of attack $\alpha = 20°$, which corresponds to the operating condition generating the highest thrust for crescent-shaped wingsails. This arrangement allows the study of aerodynamic interaction and load distribution among the wingsails under realistic operating conditions.

### 2.2 CFD simulation

The aerodynamic performance of the triple-wingsail system is evaluated using three-dimensional computational fluid dynamics (CFD) simulations. The simulations are performed using the commercial software STAR-CCM+ (Siemens PLM Software, 2021).

It should be mentioned that the CFD methodology adopted in the present study has been validated against wind-tunnel measurements in previous studies on the same crescent-shaped wingsail geometry (Zhu, 2024). Those studies compared aerodynamic force coefficients obtained from IDDES simulations with model-scale wind-tunnel experiments and further examined Reynolds-number sensitivity and scale effects. The validation showed that the numerical approach can reproduce the main aerodynamic trends and force characteristics of crescent-shaped wingsails. However, it should be noted that the present CFD and FSI simulations are performed at full scale, whereas the available wind-tunnel data were obtained on a model scale. Therefore, a direct quantitative comparison between the present full-scale results and the model-scale experiments is not appropriate, since previous Reynolds-number sensitivity studies showed that the lift coefficient at full scale can be significantly higher than that at model scale because the laminar–turbulent transition and the resulting separation/reattachment patterns are different (Zhu, 2024). For this reason, the experimental data is not directly plotted against the present full-scale FSI results.

#### 2.2.1 Computational domain and boundary conditions

The computational domain is constructed as a rectangular volume surrounding the wingsail system, following previous studies (Zhu *et al.*, 2024b), as illustrated in **Figure 2**(a). The upstream boundary is located sufficiently far from the sails to ensure a fully developed inlet flow, while the downstream boundary is extended to capture the wake development behind the sails. The distance between the sail tip and the top boundary of the computational domain is set to four times the sail span, allowing realistic development of tip vortices.

A uniform velocity inlet boundary condition is applied at the upstream panel, representing the incoming apparent wind with velocity $V_\infty = 8\ \mathrm{m/s}$. The downstream, top, and lateral panels are

defined as a pressure outlet. The bottom boundaries are treated as symmetrical planes. The wingsail surfaces are set as no-slip walls.

### 2.2.2 Discretization and numerical mesh

Second-order spatial discretization schemes are employed for both momentum and turbulence equations to improve numerical accuracy. The computational domain is discretized using unstructured meshes with a trimmed-cell topology, as shown in **Figure 2**, which provides good numerical stability and flexibility for complex geometries.

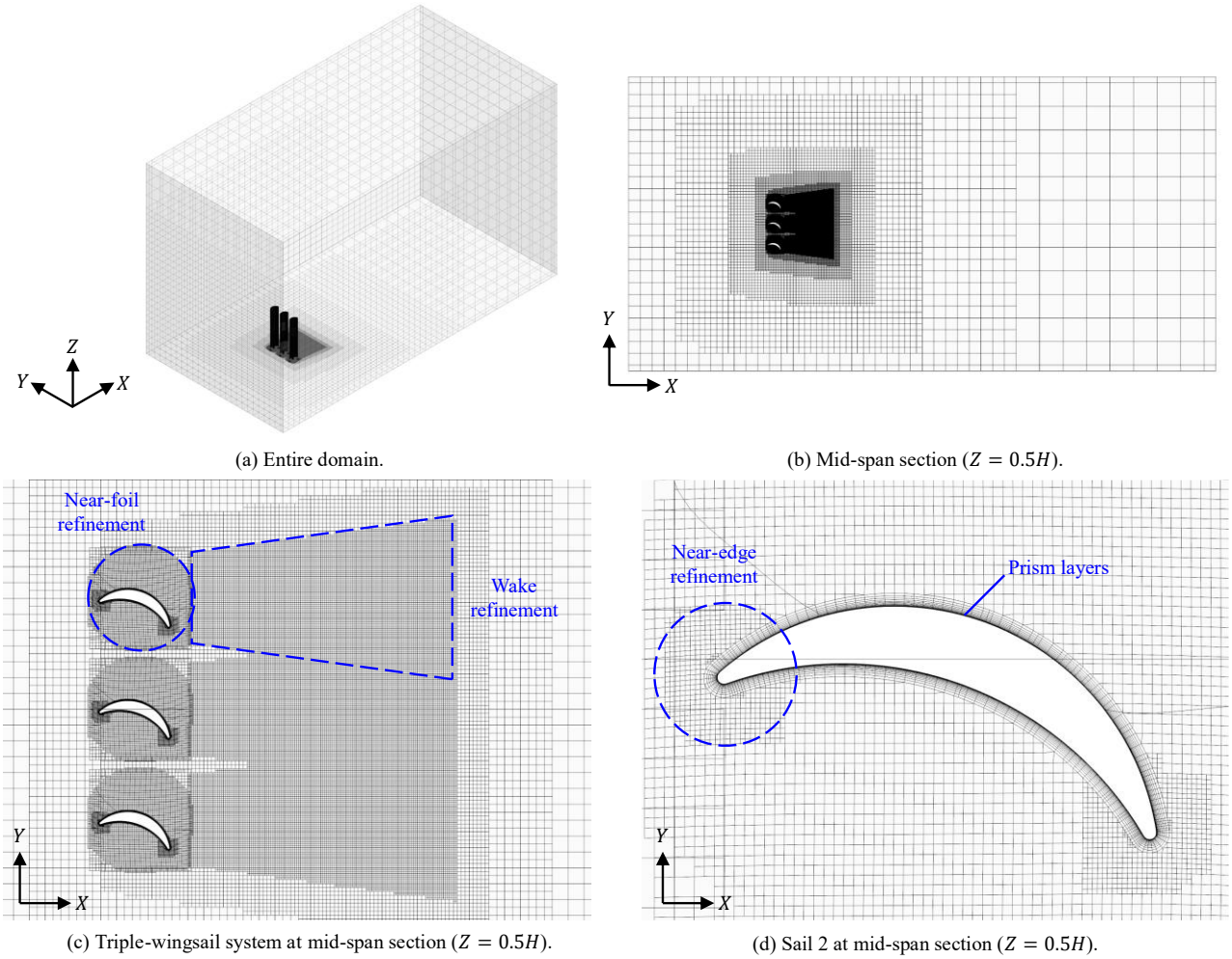


(a) Entire domain.

(b) Mid-span section ($Z = 0.5H$).

(c) Triple-wingsail system at mid-span section ($Z = 0.5H$).

(d) Sail 2 at mid-span section ($Z = 0.5H$).

**Figure 2**. Numerical mesh of the fluid domain.

Mesh refinement is applied in several critical regions to capture the main flow features. A detailed mesh convergence and numerical sensitivity analysis for the present wingsail configuration has been performed in previous studies (Nikmanesh, 2021; Zhu *et al.*, 2022; Zhu *et al.*, 2023c), including systematic investigations of mesh refinement strategy, target mesh size, mesh topology (trimmed *vs.* polyhedral), time-step size, and the number of internal iterations per time step. These studies demonstrated that the adopted mesh and numerical settings provide mesh-independent aerodynamic force predictions and adequately resolve the relevant flow structures. A refined mesh is applied around the wingsail surfaces to accurately resolve the boundary layer and near-wall flow structures. Prism layers are generated along the sail surfaces to properly capture the velocity gradients in the boundary layer region. The prism layer system consists of 14 layers with a total thickness of $0.4$ m and a first-layer thickness of $0.005$ m. This mesh configuration also ensures that the near-wall flow structures are properly captured, as the near-wall resolution satisfies

dimensionless wall distance $y^+ < 5$ over the entire wingsail surface, with more than $90\%$ of the wall cells having $y^+ < 1$, which ensures that the boundary layer is well resolved within the hybrid RANS–LES framework. Besides, additional mesh refinement is introduced near the leading and trailing edges of the wingsail profile to resolve strong pressure gradients and flow separation phenomena. A wake refinement region is defined downstream of the sails to accurately capture vortex shedding and wake interactions between the sails.

The mesh resolution gradually coarsens away from the wingsails to reduce computational cost while maintaining sufficient accuracy in the regions of interest. The global refinement level is based on mesh independence verification conducted in previous studies (Nikmanesh, 2021; Zhu *et al.*, 2023c), the total number of cells is around 18 million.

#### 2.2.3 Turbulence model and solver

The flow field is solved using a finite-volume-based CFD solver. The incompressible Navier–Stokes equations are solved under unsteady conditions. Turbulence effects are modeled using improved delayed detached eddy simulation (IDDES) (Shur *et al.*, 2008), a hybrid RANS–LES turbulence model, to capture both attached boundary layer flow and large-scale separated structures. For the URANS region, the $k$–$\omega$ shear stress transport (SST) turbulence model (Menter, 1993) is applied. A blended wall treatment approach is adopted to ensure robustness for complex geometries and varying wall-distance conditions.

The pressure–velocity coupling is handled using a segregated solver. The pressure–velocity coupling is solved using the SIMPLE algorithm (Patankar, 1980). The number of internal iterations within one time step is ten. The scale of time steps is $0.001\ \mathrm{s}$, ensuring the Courant–Friedrichs–Lewy (CFL) number lower than $10$, while for more than $99\%$ of the computational domain the CFL number is below $1$. This ensures sufficient temporal resolution for capturing unsteady flow structures while maintaining numerical stability and efficiency.

### 2.3 FEA and FSI coupling

The structural deformation of the wingsails and their interaction with the surrounding airflow are investigated using a two-way coupled FSI approach. The FSI framework follows the methodology previously developed for a single crescent-shaped wingsail (Zhu *et al.*, 2024a). The present study extends this approach to a triple-wingsail configuration, while maintaining the same numerical strategy for structural modelling and coupling between the fluid and structural solvers.

To make the coupled simulations computationally feasible, a simplified structural representation of the wingsails is adopted. Following the approach proposed by Zhu *et al.* (2024a), the complex internal structure of the real wingsail is replaced by a simplified solid model that preserves the same bending stiffness as the physical structure. In practical wingsail designs, the structure typically consists of internal frames, vertical stiffeners, and lightweight panels that carry distributed aerodynamic loads (Zhu *et al.*, 2023a). However, modelling these components explicitly would significantly increase the computational cost and decrease the stability of simulation. Therefore, to facilitate the coupled FSI simulations, the structural model of each wingsail is represented by an equivalent continuum model that preserves the global bending stiffness of the real structure. Specifically, the detailed internal structure, consisting of frames, stiffeners, and panels, is replaced by a simplified solid model with equivalent bending rigidity, expressed through the product $EI$, where $E$ is the effective Young's modulus and $I$ is the area moment of inertia of the cross-section. This approach ensures that the global deformation behavior of the wingsail under aerodynamic loading is accurately reproduced while maintaining computational efficiency.

The structural response of the wingsails under aerodynamic loading is computed using dynamic finite element analysis (FEA). As in the single-wingsail study (Zhu *et al.*, 2023a), a dynamic FEA

formulation is adopted in order to capture the structural response to unsteady aerodynamic loads. The structural dynamics of the wingsail are governed by

$$M\ddot{\lambda} + C\dot{\lambda} + K\lambda = F, \tag{1}$$

where $M$ is the mass matrix, $C$ is the damping matrix, $K$ is the stiffness matrix, and $F$ represents the aerodynamic loads acting on the structure. The displacement vector $\lambda$ describes the deformation of the wingsail surface. The aerodynamic pressure and shear stresses calculated from the CFD solver (Section 2.2) are transferred to the structural model as external loads. The resulting structural deformation is then computed by solving the dynamic equilibrium equation at each time step. The structural response is solved using the built-in finite element solver in STAR-CCM+, which is directly coupled with the CFD solver within the same simulation environment.

The dynamic response of the wingsail is governed by its modal properties, which are determined by the effective mass, stiffness, and damping of the structure (Rao & Yap, 1995). In particular, according to Zhu *et al.* (2024a), the fundamental natural frequency plays a dominant role in the aeroelastic response observed in the present study. Following classical beam theory, the first-mode natural frequency can be approximated as a function of effective bending stiffness and mass distribution along the span.

To capture the aeroelastic interaction between airflow and structural deformation, a two-way coupled FSI approach is employed. In this framework, the CFD solver first calculates the aerodynamic loads acting on the wingsail surface. These loads are transferred to the structural solver, where the structural deformation is obtained through FEA. The resulting displacements are then fed back to the CFD solver to update the fluid mesh and modify the flow field. This exchange of information continues iteratively at every time step until convergence is achieved for both the fluid and structural solutions. The mesh deformation during the FSI simulations is handled using a radial basis function (RBF) morphing method within an arbitrary Lagrangian–Eulerian (ALE) framework. Compared with one-way coupled FSI, this two-way coupling accounts for the influence of structural deformation on the flow field, which is essential for accurately capturing aeroelastic phenomena such as deformation-induced lift reduction and flutter behavior observed in flexible wingsails.

## 3. Results and discussion

### 3.1 Aeroelastic effects on structural responses

The aeroelastic deformation of the wingsails is quantified using the time-averaged tip displacements in the streamwise and crossflow directions, denoted as $\langle\lambda_X\rangle$ and $\langle\lambda_Y\rangle$, respectively. **Figure 3** presents the mean values and standard deviations of the tip displacements under three apparent wind angles ($\beta = 60°, 90°, 120°$). To provide a scale-independent perspective, the magnitude of the tip displacement is on the order of $10^{-3}$ of the spanwise length. However, due to the large wingsail height ($L_s = 74\ \mathrm{m}$), the absolute tip displacement remains significant in practical terms. For this reason, the results in **Figure 3** are presented in absolute values.

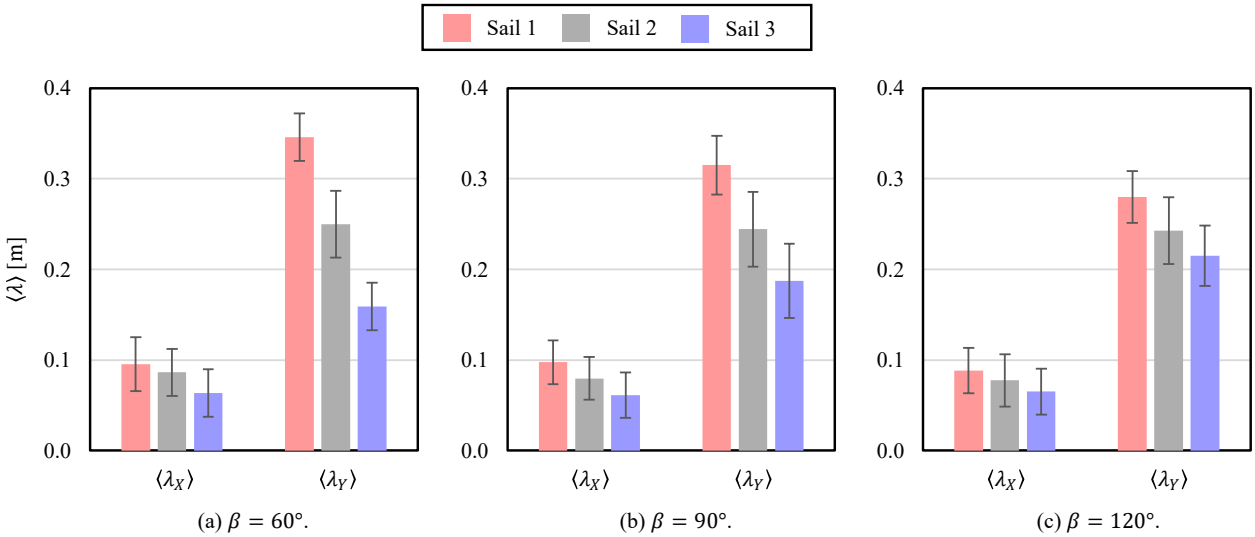


(a) $\beta = 60°$. (b) $\beta = 90°$. (c) $\beta = 120°$.

**Figure 3**. $\langle\lambda_X\rangle$ and $\langle\lambda_Y\rangle$ at different apparent wind angles. $\langle\lambda_X\rangle$ is the time-averaged tip displacement in the $X$ direction, and $\langle\lambda_Y\rangle$ is the time-averaged tip displacement in the $Y$ direction. Error bars represent the standard deviation.

For all wind angles, the crossflow displacement $\langle\lambda_Y\rangle$ is considerably larger than the streamwise displacement $\langle\lambda_X\rangle$, while the resulting total displacement vector is observed to be approximately perpendicular to the chord line of the wingsail. This suggests that the structural deformation is primarily governed by the resultant aerodynamic force acting on the wingsail. Such behavior is consistent with previous studies on wingsail aerodynamics (Zhu *et al.*, 2024b; Zhu *et al.*, 2023c), where the resultant aerodynamic force, formed by the combination of lift and drag, was found to be oriented nearly normal to the chord line.

A clear difference in structural response can also be observed among the three wingsails. The upstream wingsail (Sail 1) consistently exhibits the largest deformation, while the downstream wingsail (Sail 3) shows the smallest displacement. This behavior is mainly associated with the aerodynamic interaction between the wingsails. The upstream wingsail modifies the incoming flow field and generates wake structures that interact with the downstream wingsails. As a result, the aerodynamic loads experienced by the downstream wingsails are reduced, leading to smaller structural deformation. This interaction effect is most pronounced at $\beta = 60°$. At this apparent wind angle, the angle between the wind direction and the vessel centerline, which coincides with the arrangement direction of the wingsails, is relatively small. Consequently, the downstream wingsails are more directly exposed to the disturbed wake generated by the upstream wingsails, enhancing the aerodynamic interaction.

In addition to the mean deformation, the error bars in **Figure 3** indicate noticeable fluctuations in the structural response, particularly for the transverse displacement. These fluctuations originate from the unsteady aerodynamic forces associated with vortex shedding and wake interaction between the sails. The coupling between these unsteady flow structures and the flexible wingsails results in time-varying aerodynamic loads and corresponding structural oscillations.

Taking the case with $\beta = 60°$ as an example, the time histories of the tip displacement presented in **Figure 4** show a clear periodic oscillatory behavior for all three sails. After the initial transient phase, the structural response reaches an oscillatory state with a relatively stable amplitude and period. The three wingsails exhibit very similar oscillation frequencies, indicating that the dynamic response of the wingsail array is dominated by a common excitation mechanism rather than independent structural behavior.

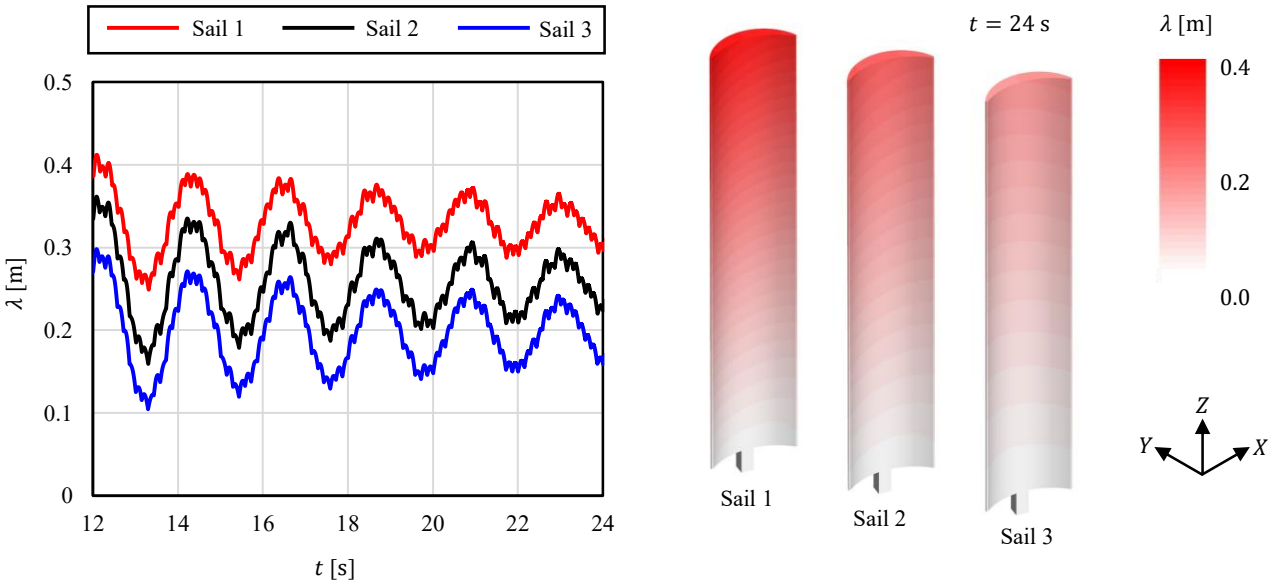


**Figure 4**. Time history of the total tip displacement and the distribution of total displacement at $t = 24$ s. $\beta = 60°$.

Spectral analysis of the displacement signals further reveals that the dominant frequency of the response is close to the natural frequency of the wingsail structure ($\sim 0.45$ Hz (Zhu *et al.*, 2024a)). This suggests that the aerodynamic forcing induced by the unsteady flow around the wingsails excites the structural vibration near its fundamental mode. Such frequency alignment indicates that the fundamental structural mode strongly contributes to the observed response. Although the downstream wingsails (Sail 3) exhibit smaller time-averaged displacements, the fluctuation amplitude, as indicated by the error bars, is relatively larger compared with the others. This behavior is associated with the stronger unsteady aerodynamic forcing caused by wake interaction.

### 3.2 Aeroelastic effects on wind loads

**Figure 5** compares the time-averaged aerodynamic force coefficients obtained from pure CFD simulations (rigid body assumption) and FSI simulations where structural deformation is taken into account. Overall, the aeroelastic response slightly modifies the aerodynamic performance of the wingsails, although the magnitude of the change depends on the sail position and wind angle.

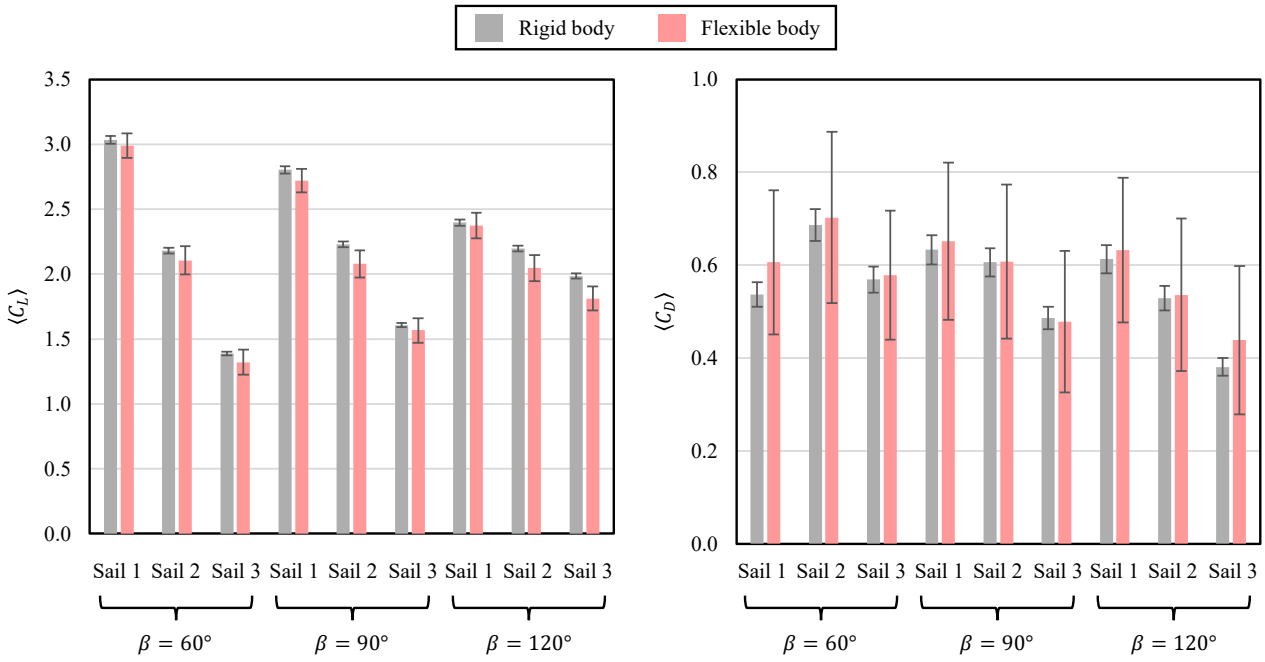


**Figure 5**. Time-averaged force coefficients according to pure CFD simulations (rigid body) and FSI analyses (flexible body).

For the lift coefficient, the differences between the rigid and flexible cases are generally small. In several cases, such as Sail 1 at $\beta = 60°$, the flexible configuration produces a slightly higher lift, while in other cases the lift decreases slightly. This indicates that the structural deformation alters the effective aerodynamic shape of the wingsail, which may either increase or decrease the pressure difference across the sail depending on the local flow conditions. The drag coefficient exhibits a somewhat larger sensitivity to aeroelastic deformation. For most cases, the flexible-body simulations show slightly higher drag values and larger fluctuations, as indicated by the error bars. This behavior suggests that structural deformation can modify the flow separation and wake development around the sails. It is also observed that the downstream sails tend to experience larger variations in both lift and drag when flexibility is considered. This can be attributed to the stronger aerodynamic interaction and wake disturbances generated by the upstream sails, which amplify the sensitivity of the downstream sails to structural deformation. This result indicates that the deformation effectively modifies the camber and local angle of attack of the wingsail, thereby altering the pressure distribution and wake structure.

To quantify the influence of aeroelastic deformation, the relative differences between the rigid-body (pure CFD) and flexible-body (FSI) simulations are evaluated. The lift coefficients show a reduction ranging from approximately $-1.5\%$ to $-8.7\%$, with an average decrease of about $-4.3\%$. The drag coefficient exhibits a wider variation, ranging from $-1.5\%$ to $15.1\%$, also with an average increasement of approximately $4.3\%$. The magnitude of the aeroelastic effect depends on both the apparent wind angle and the sail position. The differences are comparable at $\beta = 60°$ and $90°$, while the largest deviations are observed at $\beta = 120°$, where flow separation and unsteady effects are more pronounced. In terms of sail position, the upstream sail (Sail 1) shows the smallest deviation, while the downstream sails (Sail 2 and especially Sail 3) exhibit larger differences. This trend reflects the increasing influence of wake interaction and unsteady aerodynamic forcing along the sail array.

To further examine the influence of aeroelasticity on the aerodynamic performance, the spanwise distributions of the time-averaged force coefficients along the wingsails are analyzed. **Figure 6** presents the lift and drag coefficients of the four structural segments for the three sails under different apparent wind angles.

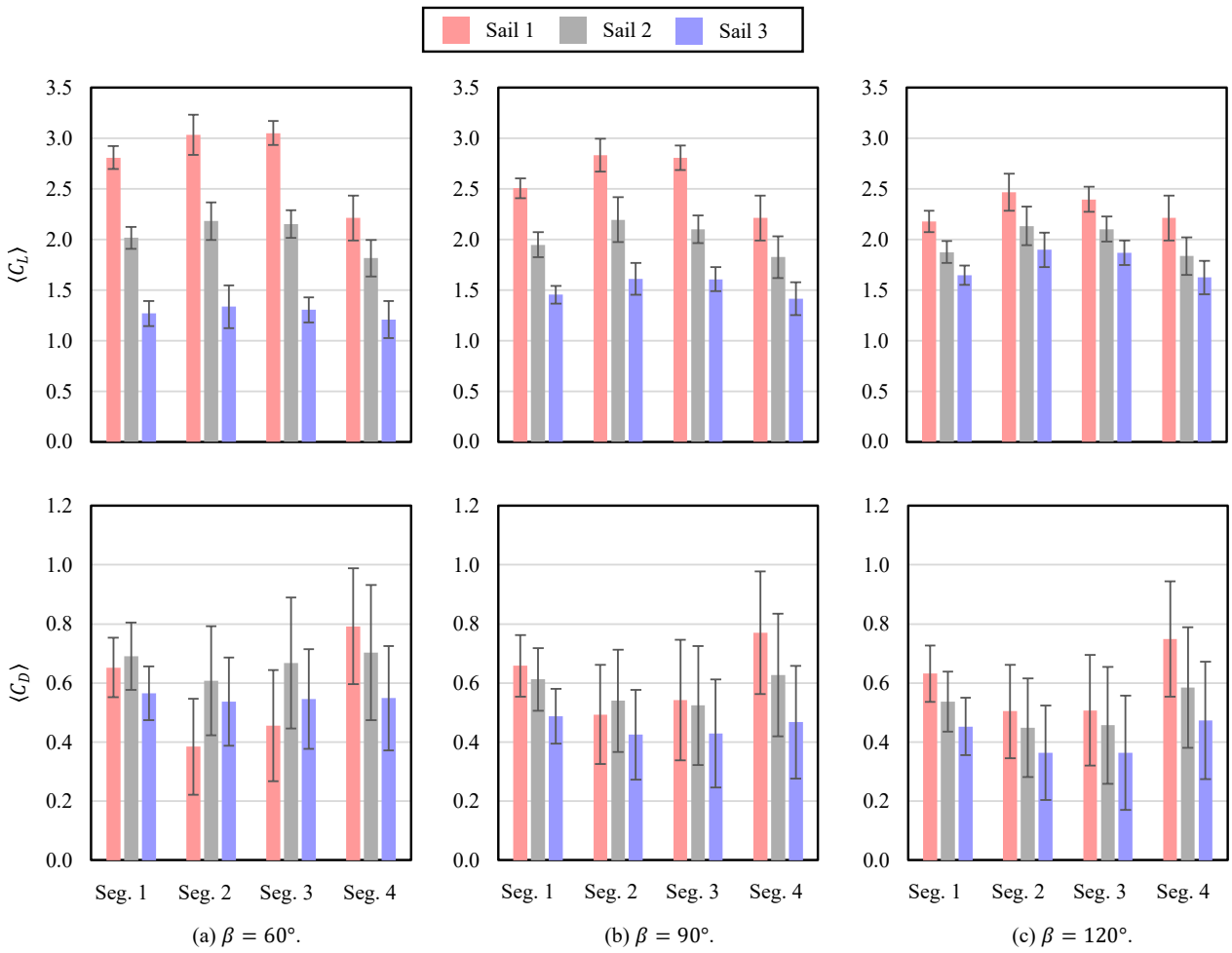


**Figure 6**. Time-averaged force coefficients of each wingsail segment according to FSI analyses (flexible body).

For all wind angles, the upstream wingsail (Sail 1) consistently produces the largest lift coefficients across most segments, while the downstream wingsail (Sail 3) exhibits the lowest lift levels. This trend reflects the aerodynamic interaction within the wingsail array, where the upstream wingsail modifies the incoming flow and reduces the effective inflow velocity experienced by the downstream sails.

The lift distribution along the span is generally non-uniform. Higher lift values are typically observed in the middle segments (Seg. 2 and Seg. 3), whereas the top and bottom segments produce relatively lower lift. This behavior can be attributed to three-dimensional flow effects, including tip vortices and the influence of the supporting structure near the base (Zhu *et al.*, 2024b). The drag distribution shows a similar spanwise variation, although the differences between wingsails are less pronounced compared with the lift distribution. In addition, the error bars indicate that the load fluctuations are generally larger in the upper segments, suggesting stronger unsteady aerodynamic effects near the wingsail tip.

## 4. Conclusions

This study investigates the aeroelastic behavior of a triple-wingsail system using a two-way coupled FSI framework. The aerodynamic flow field is resolved using computational fluid dynamics with IDDES turbulence model, while the structural response of the wingsails is computed using dynamic FEA. Three apparent wind angles representative of practical ship operation ($\beta = 60°$, $90°$, and $120°$) are considered. The results provide insights into aerodynamic interaction among multiple

wingsails, the resulting structural deformation patterns, and the influence of aeroelasticity on aerodynamic loads and propulsion performance.

The simulations show that noticeable aeroelastic deformation occurs in the wingsail system under aerodynamic loading. The crossflow displacement is significantly larger than the streamwise displacement, and the resulting deformation direction is approximately perpendicular to the wingsail chord line. This observation indicates that the structural response is mainly governed by the resultant aerodynamic force acting on the wingsail. Clear differences are also observed among the three wingsails. The upstream wingsail consistently exhibits larger deformation due to aerodynamic interaction and wake disturbances generated by the downstream wingsails. The structural response also shows periodic oscillations whose dominant frequency is close to the natural frequency of the wingsail structure, indicating strong fluid–structure coupling between unsteady aerodynamic loads and structural dynamics.

The aeroelastic deformation also influences the aerodynamic performance of the wingsail system. Comparisons between rigid-body CFD simulations and flexible-body FSI simulations indicate that the mean lift coefficients are only slightly affected by structural deformation, whereas the drag coefficients show somewhat larger sensitivity. Structural deformation modifies the effective camber and local angle of attack of the wingsail, thereby altering the pressure distribution and wake development. In addition, the spanwise load distributions show that the middle segments of the wingsail generally generate higher lift, while the tip and root regions experience lower aerodynamic loads due to three-dimensional flow effects.

Overall, the results demonstrate that aeroelastic effects should be considered when predicting the aerodynamic performance of multi-wingsail propulsion systems. Although the influence on mean lift remains relatively moderate, structural flexibility modifies load distribution, drag characteristics, and unsteady aerodynamic behavior, particularly for downstream sails affected by wake interaction. Future work should investigate a wider range of operating conditions, including different sail spacing, wind speeds, and ship motions, and explore design strategies to improve the aeroelastic stability and propulsion efficiency of large-scale wingsail installations.

**References**

Atkinson, G. M. (2019). Analysis of lift, drag and CX polar graph for a 3D segment rigid sail using CFD analysis. *Journal of Marine Engineering and Technology*, *18*(1), 36-45.

Engström, P., Xu, K., & Bensow, R. (2025). Performance Enhancement of Multiple Wingsail Airfoils Using Co-flow Jet Active Flow Control. AIAA SCITECH 2025 Forum,

Hillenbrand, A., Giovannetti, L. M., Dhomé, U., & Kuttenkeuler, J. (2024). Wind Tunnel Tests of a Two-Element Wingsail with Focus on Near-Stall Aerodynamics. *Journal of Sailing Technology*, *9*(01), 110-127.

Hu, Y., He, J., Tang, J., Xue, S., Liu, S., & Wu, Y. (2015). Sail Structure Design and Stability Calculation for Sail-assisted Ships. Marine Engineering Frontiers,

Huang, J., & Souppez, J.-B. (2025). State of the Art in Wind Assisted Ship Propulsion for Maritime Decarbonisation and Sustainable Shipping: A Systematic Review. *Journal of Sailing Technology*, *10*(01), 258-278.

IMO. (2023). IMO Strategy on Reduction of GHG Emissions from Ships. In.

Lu, R., & Ringsberg, J. W. (2020). Ship energy performance study of three wind-assisted ship propulsion technologies including a parametric study of the Flettner rotor technology. *Ships and Offshore Structures*, *15*(3), 249-258.

Ma, R., Li, D., Zhang, R., Tian, F., Tang, Z., Cao, J., Xie, Y., Jing, Z., Chen, J., & Li, X. (2025). Arrangement optimization of wingsails subject to complex mutual aerodynamic interference: A numerical study. *Ocean Engineering*, *342*, 122919.

Malmek, K., Larsson, L., Werner, S., Ringsberg, J. W., Bensow, R., & Finnsgård, C. (2024). Rapid aerodynamic method for predicting the performance of interacting wing sails. *Ocean Engineering*, *293*, 116596.

Mebratu, M. M., Hectors, K., & De Waele, W. (2026). Comparative Analysis of Wind Load Application Techniques for Aeroelastic Analysis of Hard Wingsails. *Journal of Sailing Technology*, *11*(01), 95-114.

Menter, F. R. (1993). Zonal two equation κ-ω turbulence models for aerodynamic flows. AIAA 23rd Fluid Dynamics, Plasmadynamics, and Lasers Conference, Orlando,FL,U.S.A.

Nikmanesh, M. (2021). *Sailing performance analysis using CFD simulations: A study on crescent shaped wing profiles* Chalmers University of Technology]. Gothenburg, Sweden. https://odr.chalmers.se/handle/20.500.12380/304303

Ouchi, K., Uzawa, K., & Kanai, A. (2011). Huge Hard Wing Sails for the Propulsor of Next Generation Sailing Vessel. Second International Symposium on Marine Propulsors, Hamburg, Germany.

Ouchi, K., Uzawa, K., Kanai, A., & Katori, M. (2013). Wind challenger" the next generation hybrid sailing vessel. The Third International Symposium on Marine Propulsors, Launceston, Tasmania, Australia, Launceston, Tasmania, Australia.

Patankar, S. V. (1980). *Numerical heat transfer and fluid flow*. CRC Press. https://doi.org/10.13182/nse81-a20112

Persson, A., Li, D. Q., Olsson, F., Werner, S., & Dhomé, U. (2019). Performance prediction of wind propulsion systems using 3D CFD and route simulation. RINA, Royal Institution of Naval Architects-International Conference on Wind Propulsion, WP 2019, 15-16 October 2019, London, United Kingdom,

Rao, S. S., & Yap, F. F. (1995). *Mechanical vibrations* (Vol. 4). Addison-Wesley New York.

Reche-Vilanova, M., Hansen, H., & Bingham, H. B. (2021). Performance prediction program for wind-assisted cargo ships. *Journal of Sailing Technology*, *6*(01), 91-117.

Shur, M. L., Spalart, P. R., Strelets, M. K., & Travin, A. K. (2008). A hybrid RANS-LES approach with delayed-DES and wall-modelled LES capabilities. *International Journal of Heat and Fluid Flow*, *29*(6), 1638-1649.

Siemens PLM Software. (2021). STAR-CCM+ user guide (version 16.02). In: Siemens PLM Software Inc: Munich, Germany.

Souppez, J.-B. (2023). Structural Challenges of Low-Emission Vessels: A Review. *International Journal of Maritime Engineering*, *165*(A2), 165-178 %@ 1479-8751.

Storhaug, G., Borzacchiello, G. R., & Hoffmeister, H. (2022). Fatigue assessment of wind assisted propulsion systems. Proceedings of the ASME 2022 41st Internal Conference on Ocean, Offshore and Arctic Engineering,

Thies, F., & Fakiolas, K. (2022). Wind propulsion. In *Sustainable Energy Systems on Ships* (pp. 353-402). Elsevier.

van Reen, S., Zhu, H., Lin, J., Niu, J., Sharpe, P., & Yao, H.-D. (2025). Aerodynamic optimization of in-line and parallel layouts for symmetric cambered wingsail installation. International Conference on Offshore Mechanics and Arctic Engineering,

Xu, K., Malmek, K., & Bensow, R. (2025). Numerical investigation of multiple wingsails interaction under different apparent wind angles. *Ocean Engineering*, *336*, 121712.

Zeng, Q., Zhang, X., Cai, W., & Zhou, Y. (2023). Wake distortion analysis of a Dynarig and its application in a sail array design. *Ocean Engineering*, *278*, 114341.

Zhang, R., Huang, L., Chen, J., Peng, G., Ma, R., Cao, J., Wang, C., Wu, J., & Li, X. (2025). A novel energy conservation method for wind-assisted propulsion ships based on sails thrust optimization. *Energy*, 139025.

Zhang, R., Huang, L., Ma, R., Peng, G., Ruan, Z., Wang, C., Zhao, H., Li, B., & Wang, K. (2024). Numerical investigation on the effects of heel on the aerodynamic performance of wing sails. *Ocean Engineering*, *305*, 117897.

Zhang, R., Huang, L., Peng, G., Ma, R., Wang, K., Tian, F., & Song, Q. (2023). A novel method of desynchronized operation of sails for ship wind-assisted propulsion system. *Ocean Engineering*, *288*, 115964.

Zhu, H. (2023). *Methods for the Evaluation of Wingsails with a Crescent-shaped Profile* Chalmers University of Technology]. Gothenburg, Sweden.

Zhu, H. (2024). *Analysis and evaluation of wingsails with crescent-shaped profiles: from aerodynamics to aeroelasticity* Chalmers University of Technology]. Gothenburg, Sweden.

Zhu, H., Bikkireddy, S., Ringsberg, J. W., & Yao, H.-D. (2023a). Structure analysis of lightweight sail structures for wind-assisted ship propulsion. 9th International Conference on Marine Structures , MarStruct, Gothenburg, Sweden.

Zhu, H., Chernoray, V., Yao, H.-D., Ringsberg, J. W., & Ramne, B. (2023b). Experimental study on structure responses of triple wing sails to turbulence flows at multiple apparent wind angles. 9th International Conference on Marine Structures , MarStruct, Gothenburg, Sweden.

Zhu, H., Chernoray, V., Yao, H.-D., Ringsberg, J. W., & Ramne, B. (2024a). Fluid-structure interaction analysis of crescent-shaped wingsails. Proceedings of the International Conference on Offshore Mechanics and Arctic Engineering - OMAE, Singapore, Singapore.

Zhu, H., Nikmanesh, M. B., Yao, H. D., Ramne, B., & Ringsberg, J. W. (2022). Propulsive Performance of a Novel Crescent-Shaped Wind Sail Analyzed With Unsteady Rans. Proceedings of the International Conference on Offshore Mechanics and Arctic Engineering - OMAE, Hamburg, German.

Zhu, H., Yao, H.-D., & Ringsberg, J. W. (2024b). Unsteady RANS and IDDES studies on a telescopic crescent-shaped wingsail. *Ships and Offshore Structures*, 1-14.

Zhu, H., Yao, H.-D., Thies, F., Ringsberg, J. W., & Ramne, B. (2023c). Propulsive performance of a rigid wingsail with crescent-shaped profiles. *Ocean Engineering*, *285*, 115349.